MID-IR LASER ABSORPTION SPECTROSCOPY MEASUREMENTS OF TEMPERATURE AND CARBON MONOXIDE IN A ROTATING DETONATION ROCKET ENGINE

by

Matthew G. Blaisdell

A Thesis

Submitted to the Faculty of Purdue University

In Partial Fulfillment of the Requirements for the degree of

Master of Science

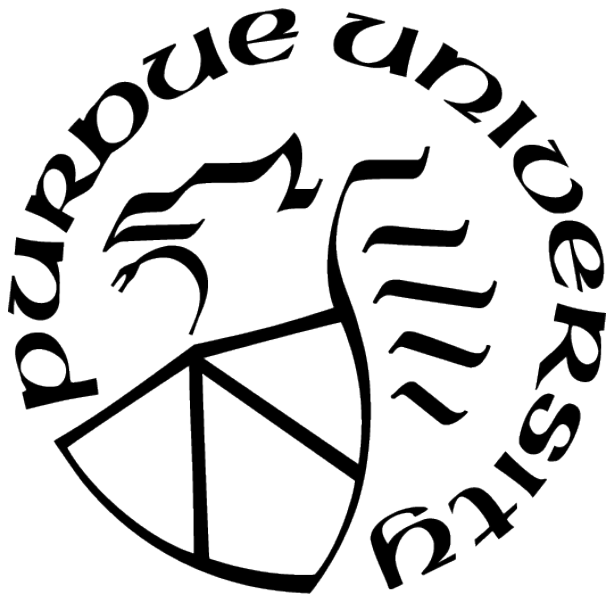

School of Mechanical Engineering

West Lafayette, Indiana

May 2021

THE PURDUE UNIVERSITY GRADUATE SCHOOL
STATEMENT OF COMMITTEE APPROVAL

Dr. Christopher S. Goldenstein, Chair

School of Mechanical Engineering

and School of Aeronautics and Astronautics (by courtesy)

Dr. Robert P. Lucht

School of Mechanical Engineering

and School of Aeronautics and Astronautics

Dr. Steven F. Son

School of Mechanical Engineering

and School of Aeronautics and Astronautics (by courtesy)

Approved by:

Dr. Nicole Key

ACKNOWLEDGMENTS

I have had the severe good fortune to have had a great many people lend me a vast amount of help throughout my life and my time at Purdue. Without them all I surely would not have made it this far, and so this accomplishment belongs to them too.

I owe an enormous debt of gratitude to my advisor, Prof. Chris S. Goldenstein. He has been a constant source of encouragement since I started working with the Goldenstein Group as an undergraduate student. He has always been willing to share his time and has been very patient with me while enthusiastically reminding me of what I am capable of and pushing me to achieve it.

I would also like to thank Dr. Robert P. Lucht and Dr. Steven F. Son for serving on my thesis committee.

I would like to thank Aaron Lemcherfi for running the engine test campaign and all of his assistance during that, as well as Dr. Carson D. Slabaugh and the rest of his research group for all of their help too. I would also like to thank Dr. Keith Rein of Spectral Energies for his assistance during testing.

It has also been a pleasure to get to know and work alongside the diligent and friendly members of the Goldenstein Group (Austin McDonald, Garrett Mathews, Morgan Ruesch, Ryan Tancin, Vishnu Radhakrishna, and Ziqiao Chang). I have learned a lot just from talking with you all. I would especially like to thank Garrett Mathews. He has been a mentor to me from the start and I would know a lot less about laser diagnostics if it wasn't for him. He has also been a huge source of support for me during this work.

I also have a lot to thank my family for. My parents were the ones to foster my curiosity in how things worked and I definitely owe them for my "engineering genes". Additionally, I would like to thank my parents for housing, feeding, and loving me and for letting me talk as much or as little about lasers as I needed to. My father has been a source of knowledge for me as I have been navigating graduate school and my mother has consistently provided encouraging reminders and occasionally helpful (if accidental) distractions. I would also like to thank the rest of my family for their support, encouragement, and care, particularly Marissa, Ginny, and Abby.

This work was supported by Grant FA9300-19-P-1506 with Dr. John W. Bennewitz of the Air Force Research Laboratory (AFRL) as program monitor and AFOSR Grant FA9550-18-1-0210 with Dr. Mitat Birkan as program manager. I would like to thank Dr. Chiping Li of the Air Force Office of Scientific Research (AFOSR) for helping support the operation of test facilities through Grant FA9550-16-1-0534. I would also like to thank Dr. William A. Hargus Jr. and Dr. John W. Bennewitz of AFRL for thoughtful discussions throughout the project.

This material is based upon work supported by the National Science Foundation Graduate Research Fellowship Program under Grant No. DGE-1842166. Any opinions, findings, and conclusions or recommendations expressed in this material are those of the author(s) and do not necessarily reflect the views of the National Science Foundation.

TABLE OF CONTENTS

LIST OF TABLES

LIST OF FIGURES

LIST OF SYMBOLS

α	absorbance
I_t	transmitted intensity
I_0	incident intensity
$S(T)$	linestrength
X	mole fraction
P	pressure
ϕ	lineshape
L	path length
ν	frequency
ν_0	linecenter frequency
A	integrated absorbance
T_0	reference temperature
$Q(T)$	partition function
E	lower-state energy
h	Planck's constant
c	speed of light
k	Boltzmann's constant
M	molecular weight
FWHM	full width at half max
$\Delta\nu_D$	Doppler FWHM
$\Delta\nu_C$	collisional FWHM
γ_{B-A}	collisional-broadening coefficient
N	temperature exponent
R	ratio of integrated absorbances

ABSTRACT

Laser absorption spectroscopy has enabled fast and precise diagnostics for measuring gas conditions in a wide variety of applications. This thesis presents a high-speed mid-IR LAS diagnostic for CO and demonstrates its capabilities by taking measurements inside the annulus of a rotation detonation rocket engine. This scanned direct absorption diagnostic utilizes a quantum cascade laser to interrogate CO absorption lines near 2008.5 cm^{-1} to measure temperature, pressure, and CO at 750 kHz. This diagnostic reports precise measurements (95% CI of $< 10\%$) even at elevated temperatures (2500 K) and pressures (6 atm). The presented diagnostic is the first of its kind to permit mid-infrared measurement of CO inside an RDRE annulus at repetition rates > 100 kHz.

1. INTRODUCTION

This section was adapted from: Garrett C. Mathews, Matthew Blaisdell, Aaron I. Lemcherfi, Carson D. Slabaugh, and Christopher S. Goldenstein, "High-bandwidth laser-absorption measurements of temperature, pressure, CO, and H_2O in the annulus of a rotating detonation rocket engine," AIAA Scitech 2021 Forum [1].

Laser-absorption spectroscopy (LAS) has emerged as a powerful diagnostic for characterizing combustion gases produced by rotating detonation engines (RDEs). This largely results from its ability to provide quantitative, calibration-free measurements of temperature and key combustion products (e.g., CO, CO_2, H_2O) at high rates and with limited optical access. To name a few examples, Goldenstein et al. [2] utilized dual two-color TDLAS diagnostics and scanned-WMS-$2f/1f$ to measure temperature and H_2O concentration at 10 kHz and 50 kHz in the exhaust of an H_2-air fed RDE. The measurements were utilized to quantify the combustion efficiency of the RDE. Further, the authors were able to infer how thermal stratification in the exhaust gas increased with mass flow rate by utilizing four TDLs resonant with unique H_2O absorption transitions with unique lower-state energy. Rein et al. [3] developed and deployed the first LAS diagnostic for characterizing combustion gases within the RDE annulus. A MEMS-VCSEL was utilized to measure the absorbance spectra of H_2O at wavelengths from 1330 to 1360 nm, thereby enabling the gas temperature and concentration of H_2O to be measured at 100 kHz. A dual-core fiber bundle was utilized to pitch laser light across the annular gap and collect the backscattered light. That work built on that of Caswell et al. [4] who utilized the same fiber bundle and Fourier-domain mode-locked lasers emitting at similar wavelengths to measure temperature, pressure, H_2O mole fraction, velocity, and enthalpy at 50 kHz in a pulse-detonation combustor. More recently, Peng et al. [5] developed the first mid-infrared, single-ended LAS diagnostic for RDEs. Two TDLs emitting near 2551 and 2482 nm were utilized to access strong absorption lines in H_2O's ν_3 fundamental vibration band for improved measurement sensitivity. The lasers were frequency multiplexed using modulation frequencies of 100 and 122 kHz to provide scanned-WMS-$2f/1f$ measurements of temperature and H_2O concentration at 20 kHz. A hollow-core fiber-bundle was utilized to deliver laser light to a cage assembly holding optics to direct laser light into the RDE and collect backscattered laser light onto a photodetector.

Cassady et al. [6] later expanded the measurement capabilities of this diagnostic to provide simultaneous measurements of temperature, H_2O, and CO at 44 kHz in the annulus of an H_2-ethylene-fueled RDE. A chalcogenide fiber-bundle was utilized to multiplex light from two TDLs (for temperature and H_2O) and one QCL (for CO) and an optical cage assembly was used to wavelength-demultiplex light from the TDLs and QCL onto separate detectors. While highly useful, most prior LAS diagnostics for RDEs have been limited to measurement rates less than or equal to 100 kHz which is not sufficient for resolving intracycle variations in gas conditions, particularly, in rotating detonation rocket engines (RDREs).

Recently, several LAS diagnostics have been developed which are capable of measuring temperature and species at 1 MHz in harsh combustion environments [7–11]. For example, Mathews and Goldenstein [7–9] developed a two-color TDLAS diagnostic employing scanned-WMS-$2f/1f$ for measuring temperature and H_2O at 1 MHz in fireballs of energetic materials. The wavelength of each TDL was scanned across the peak of an H_2O absorption transition at 1 MHz while being modulated at either 35 or 45.5 MHz to generate the WMS harmonic signals. The use of such high modulation frequencies enabled scanned-WMS measurements to be obtained at 1 MHz and led to improved signal-to-noise ratio (SNR) compared to a more conventional WMS diagnostic employing modulation frequencies on the order of 100 kHz. In addition, Nair et al. [10] very recently acquired measurements of temperature, CO, and CO_2 at rates of 1 to 3 MHz at the exit plane of the same RDRE studied here. The authors utilized one QCL and one interband-cascade laser (ICL) equipped with bias-T circuitry in order to rapidly ($\geq$ 1 MHz) scan across several CO absorption lines near 2008.5 cm^{-1} and CO_2 lines near 2385.4 cm^{-1}.

The work presented here builds on that of Nair et al. [10–12] to provide single-ended measurements of temperature, pressure and CO at 750 kHz in the annulus of a RDRE running on methane-oxygen mixtures. In comparison to the recent work by Nair et al. [10], the work reported here presents the notable advancements that all measurements were acquired in the RDRE annulus, thereby necessitating the use of windows and posing a more optically harsh environment at ≈2x higher pressure. Measurements are presented for a test case with the RDRE operating with a CH_4-O_2 equivalence ratio of 1.77 and mass flow rate of 0.6 lb/s. The large absorbance signals (10-60%) from CO in the mid-infrared enabled high-fidelity

measurements of temperature, pressure, and CO to be obtained at 750 kHz using scanned-DA and the use of a high-bandwidth current controller enabled this diagnostic to operate without bias-T circuitry which would have made the laser more susceptible to damage via reverse biasing of its current.

2. FUNDAMENTALS

2.1 Laser Absorption

2.1.1 Beer's Law

Laser absorption spectroscopy (LAS) is one technique that exploits the frequency dependent absorption of light to determine properties of a test gas. As described by quantum mechanics, the energy levels for molecules are quantized. Only photons of light with the correct energy and frequency will be absorbed and result in a transition of the molecule from a lower energy state to a higher energy state. For a single species at modest pressures, this results in the absorption spectrum appearing as a series of lines at distinct frequencies, where each line corresponds to a specific transition from one particular state to another. These lines are not infinitely thin, but instead have a width and shape to them due to quantum mechanical uncertainty through a variety of broadening mechanisms. Laser light is absorbed according to Beer's Law, where the ratio of transmitted to incident light intensity is related to the absorbance of the gas (See equation 2.1).

$$\alpha = -\ln \frac{I_t}{I_0} \tag{2.1}$$

The total absorbance is the sum of the absorbance caused by all lines from all species present in the gas. In effect, the absorbance of a slug of gas is dependent on the species present in the gas, their concentration, the temperature and pressure of the gas, and the path length through the gas as well as how these quantities vary along the line-of-sight [13].

$$\alpha(\nu) = \int_0^L P \sum_{\mathrm{i}}^{species} X_{\mathrm{i}} \sum_{\mathrm{j}}^{line} S_{\mathrm{i,j}}(T)\phi_{\mathrm{i,j}}(\nu - \nu_{0,\mathrm{i,j}})dl \tag{2.2}$$

2.1.2 Simplifying Assumptions

Several assumptions are often made to simplify the above equation. These are: (1) that there is only one absorbing species present in the gas, or at least only one absorbing in the relevant region of the spectrum, (2) that only one line of said species' spectrum is being

interrogated, and (3) that the gas properties do not vary along the path length. In this limit Eq. 2.2 is reduced to Eq. 2.3.

$$\alpha(\nu) = S(T)XPL\phi(\nu) \tag{2.3}$$

The first two assumptions are often easily justified as absorption from trace species or the wings of other lines can be extremely small if proper precautions are taken and when this is not the case, additional lines can be added to the absorption model as needed. In practical settings the gas properties are almost never constant along the entire path length such as in the air gaps on either end of a heated gas cell or in the boundary layer of a flame. These non-uniformities can sometimes be taken into account in the model and even yield additional insight, but several investigations have shown that for many applications accounting for these line of sight non-uniformities has only a very minor effect on measurement of path-integrated quantities [13].

2.2 Spectroscopic Parameters

2.2.1 Linestrength

The magnitude of the absorbance of a line depends on the path length, the number density of the absorbing species, and the likelihood of a transition occurring between the high and low energy states. The linestrength quantifies a species' propensity to absorb light as it transitions from a given lower state to a given upper state. Ultimately, the integrated absorbance of a given line scales linearly with the transition linestrength and the linestrength is temperature dependent due to temperature altering the fractional population in both the lower and upper states. If the linestrength is known at a reference temperature T_0 (such as in the HITRAN database [14]) then it can be determined at any other temperature via a

simple temperature scaling relation, shown in Eq. 2.4, if the upper and lower states follow a Boltzmann distribution.

$$S(T) = S(T_0)\frac{Q(T_0)}{Q(T)}\exp\left[-\frac{hcE}{k}\left(\frac{1}{T}-\frac{1}{T_0}\right)\right] \times\left[1-\exp\left(-\frac{hc\nu_0}{kT}\right)\right]\left[1-\exp\left(-\frac{hc\nu_0}{kT_0}\right)\right]^{-1} \tag{2.4}$$

2.2.2 Lineshape

The lineshape (ϕ) is the shape of the absorption line and is defined to be a function whose integral from negative to positive infinity is unity. There are many different models for lineshape but the ones relevant here are Lorentzian, Gaussian, and Voigt. There are several effects that cause line broadening and one is the additional quantum mechanical uncertainty in the energy levels of the absorbing molecule caused by collisions between the absorbing molecules and other molecules present in the gas. This effect leads to a Lorentzian lineshape. Another effect leading to line broadening is the Doppler effect since individual molecules in the gas may be moving at significant speeds relative to the lab reference frame resulting in some absorption happening at frequencies other than the line center frequency. This effect leads to a Gaussian lineshape.

When both of these effects are present and can be modeled as independent of each other, the lineshape is the convolution of the two. This is called a Voigt profile. The actual convolution is often computationally expensive to calculate, and so many approximate models have been made. The Voigt profile is ultimately determined by two parameters, the Doppler width and the collisional width, given by Eq. 2.5 and Eq. 2.6, respectively. These are also the FWHM of the Gaussian and Lorentzian profiles that make up the Voigt profile.

Doppler Width

The calculation of the Doppler width is very straightforward as it only depends on the absorbing species's molar mass, the temperature, and the linecenter frequency.

$$\Delta\nu_D = \nu_0(7.1623 \times 10^{-7})\sqrt{\frac{T}{M}} \tag{2.5}$$

Collisional Width

The determination of collisional width is more complicated as in addition to temperature, it also depends on the bath gas, or all the other species present in the gas. Similar to the linestrength, the broadening coefficient (2γ) is often tabulated at a reference temperature in spectroscopic databases like HITRAN. The coefficient at other temperatures can be calculated using the temperature coefficient (N) which is sometimes tabulated in a database but is often assumed to be a particular value (such as 0.5 or 0.75) for all lines of a given species when insufficient data is available [15].

$$\Delta\nu_C = P\sum X_A 2\gamma_{B-A}(T) \tag{2.6}$$

$$2\gamma_{B-A}(T) = 2\gamma_{B-A}(T_0)\left(\frac{T_0}{T}\right)^N \tag{2.7}$$

2.3 Determination of Temperature and Species Concentration

Laser absorption spectroscopy can be used to measure the temperature and concentration of a species in a volume of gas via measurements of its absorption spectrum. This is most clearly understood by considering a two-line absorption measurement. In this method, a Voigt profile is least-squares fit to the measured lineshape of each transition to determine

the integrated absorbance for each line. The integrated absorbance is simply the integral of Eq. 2.3 across all frequencies, resulting in Eq. 2.8.

$$A = S(T)XPL \tag{2.8}$$

The two-color ratio of integrated absorbances, R, reduces to the two-color ratio of linestrengths, as shown by Eq. 2.9, which is a function of only temperature and spectroscopic constants.

$$R = \frac{A_2}{A_1} = \frac{S_2(T)XPL}{S_1(T)XPL} = \frac{S_2(T)}{S_1(T)} \tag{2.9}$$

With the two-color ratio measured, the temperature can then be calculated directly using Eq. 2.10. From this equation it can be shown that the temperature sensitivity is directly proportional to the difference in lower-state energies $(E_2 - E_1)$, which motivates the use of two lines with a large difference in E". This is very important when choosing which two lines to use in order to maximize temperature sensitivity.

$$T = \frac{\frac{hc}{k}(E_2 - E_1)}{\ln R + \ln \frac{S_2(T_0}{S_1(T_0)} + \frac{hc}{k}\frac{E_2 - E_1}{T_0}} \tag{2.10}$$

Once the temperature is found, the mole fraction of the absorbing species can be found from the integrated absorbance of either transition (i.e., A_1 or A_2) if the pressure and path length are known. If the pressure is unknown, partial pressure can still be found directly from the integrated absorbance. Greater detail on the derivation of these relations can be found in Chapter 7 of Hanson et al. [15].

3. DIAGNOSTIC

3.1 Scanned-Wavelength Direct Absorption

Scanned-wavelength direct absorption (scanned-DA) is a LAS technique where the laser's wavelength is scanned periodically across one or more absorption lines. The absorbance for each data point in time during the scan is then directly calculated by taking the negative natural log of the ratio of incident to measured laser intensity. A model for how the laser's wavelength changes during the scan is used to transform the data from absorbance-time space to absorbance-frequency space. A model for the absorbance (see Section 2.1) is then fit to this data and gas properties such as temperature and species concentration can be further calculated from the best fit parameters as mentioned in Section 2.3.

The wavelength model for the laser's scan is found by directing the laser beam through an etalon, which will produce intensity spikes in the detected laser signal when the laser's frequency is at an integer multiple of the etalon's free spectral range (FSR). The location of these spikes in time can be used to develop a relative frequency-time relationship for the laser during the scan. Note that this technique does not yield the absolute optical frequency of the laser so that must then be inferred during the fitting of the absorbance model.

3.1.1 Baseline Fitting

Analysis of scanned-DA data requires knowledge of the incident laser intensity. While this can be measured empirically, in practice that is often not practical for *in situ* measurements. Luckily, it is not necessary either as during injection current scanning both the laser's wavelength and intensity are affected. If the current is scanned linearly, then the laser's incident intensity will also change roughly linearly. This is useful as a low order polynomial model for baseline laser intensity can be fit to the non-absorbing regions of a scanned-DA signal from which the incident laser intensity during the absorbing regions of the scanned DA signal can be interpolated.

This method works very well at low scanning frequencies, but at higher frequencies the response of the laser is less linear and baseline fitting by polynomial interpolation is less

accurate. Instead, a baseline model can be made by recording a background signal without an absorbing gas present. This captures the shape of the incident laser intensity signal. Adding a scaling parameter to this baseline signal during the fitting of the absorbance model accounts for differences in non-absorbing losses between test runs and the baseline run, since such losses are nearly wavelength independent.

3.1.2 Laser Tuning Response

The magnitude of the QCL's wavelength-tuning response to current injection decreases with increasing frequency. Several tests were conducted to characterize the QCL's wavelength-tuning response. A series of sinewaves at varying frequencies were applied to the QCL while the laser beam was directed through an etalon and into the detector. Two different QCL packages were tested. Figure 3.1 shows the resulting wavelength-tuning response for both of the QCLs. Both QCLs exhibit an approximately log-linear wavelength-tuning response at lower frequencies ($\leq$ 20 kHz). For higher frequencies the tuning amplitude of both lasers drops off much more rapidly, but both QCLs still have a small usable tuning amplitude in the range of 1-2 MHz. Interestingly, while QCL 2's tuning amplitude at low frequencies is about 20% greater than QCL 1, above 800kHz QCL1 has a larger tuning amplitude making it the better choice for high frequency diagnostics, all else being equal. The exact equipment used in this characterization is detailed in Table 4.1.

3.1.3 Utilization of Up-scans Only

The standard implementation for scanned-DA is to scan with a triangle wave so that the laser's wavelength is scanned over the absorption features twice per period giving an up-scan and a down-scan measurement. However, the features of the scan occur at specified wavelengths and as there is a slight phase shift between the laser's intensity and wavelength during the scan, thus the absorption features appear off center on the recorded transmitted laser intensity signal. At low scan frequencies ($\leq$ 1 kHz) this usually isn't an issue, but as scan frequency increases, so does the phase shift. In order for there to be sufficient non-absorbing regions on either end of the scan, the laser must be scanned further to account for the phase

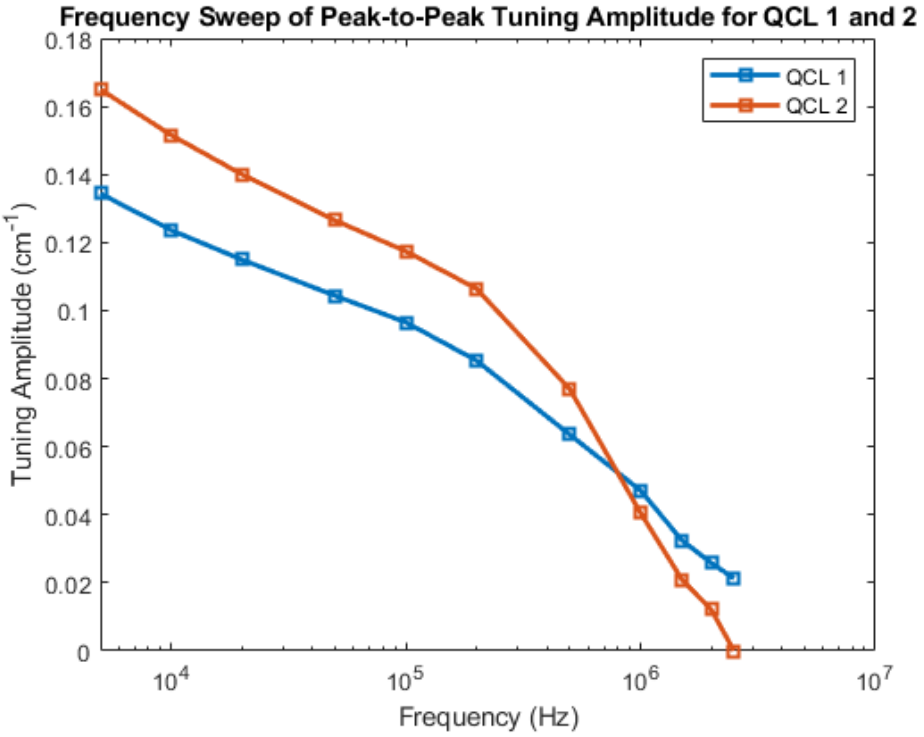

Figure 3.1. Peak-to-peak laser tuning response of two QCLs driven by a 23mApp sine wave from 5kHz to 2.5MHz

shift. However, this is somewhat wasteful, as the scans only need that additional margin on one end of the scan, but not on the other. At sufficiently high scanning frequencies it becomes impractical to try to make useful measurements on both up-scans and down-scans. A better strategy is to scan with a sawtooth wave and only take the up-scan measurements. While it does become necessary to double the scan frequency, the benefit of not having to scan as far or wasting the margin on each up/down scan outweighs the loss in tuning response.

3.2 Line Selection

Interrogating appropriate absorption lines is critical to the accuracy and precision of all LAS diagnostics. For example, the linestrength of the lines dictates signal levels, the difference in lower state energy of the lines dictates the temperature sensitivity for thermometry, the presence of absorption lines for other expected species can cause interferring absorption. Further, the laser(s) must be able to scan across the line(s) of interest at the desired measure-

ment rate. Spectraplot.com [16] was used to run simulations of various absorption spectra at expected test conditions using the HITEMP database [17]. Two candidate sections of CO's spectrum within the reach of the QCL's scanning range were identified. Lines in the area of 2008.5 cm^{-1} and 2012.7 cm^{-1} provide a good choice with details presented in Tables 3.1 and 3.2. Ultimately the lines at 2008.5 cm^{-1} were selected to be used as the presence of the fundamental line allowed for more accurate results at scan frequencies up to 1 MHz.

Table 3.1. Major CO lines near 2008.5 cm^{-1}

Transition	ν_0 [cm^{-1}]	$S(T_0)$ [cm^{-1}/(molecule cm^{-2})]	E [cm^{-1}]
P(2,20)	2008.421	1.15E-28	5051.7
P(0,30)	2008.525	2.67E-22	1901.1
P(3,14)	2008.552	2.88E-32	6742.9

Table 3.2. Major CO lines near 2012.7 cm^{-1}

Transition	ν_0 [cm^{-1}]	$S(T_0)$ [cm^{-1}/(molecule cm^{-2})]	E [cm^{-1}]
P(3,13)	2012.734	3.45E-32	6690.6
P(2,19)	2002.834	2.58E-28	4976.4

3.3 Validation Tests

A validation test of this diagnostic was performed by directing the laser light through a heated gas cell. Details on the gas cell can be found in [18]. The laser and controller equipment used in this test are listed in Table 4.1. This validation test was performed using the same QCL but scanning across a different set of lines close to 2012.7 cm^{-1} with a scan rate of 1 MHz. The purpose of this test was more so to validate a scanned-DA diagnostic with this laser at MHz frequencies. A more direct validation test focused on reproducing expected RDRE gas conditions would have required a shock tube which was not available at the time of testing. Results of the test are presented below in Table 3.3. Both temperature and concentration of CO were measured to a high degree of accuracy with $\approx 2\%$ error or

less. Furthermore, this diagnostic yielded a high degree of precision. This demonstrates the validity of using this diagnostic for frequencies up to 1 MHz.

Table 3.3. Validation Test Results

	Actual	Measured	Error
Temperature	932 K	919.2 ± 2.8 K	1.42%
X_{CO}	0.49	0.4794 ± 0.0084	2.16%

4. EXPERIMENTAL SETUP

4.1 Rotating Detonation Rocket Engine

The test platform for this study was a rotating detonation rocket engine (RDRE) designed by GHKN Engineering, LLC. This platform has been used in many previous studies by the AFRL/RQRC to test a variety of injector and chamber configurations [19–23]. For these tests, the RDRE's combustion chamber is of constant cross-section and has an outer diameter of 76 mm, a length of 76 mm, and a gap size of 5 mm with no throat or other restriction downstream. The RDRE was fueled with chemically pure (>99%) methane and industrial grade oxygen, which was ran through independent fuel and oxidizer manifolds and then fed into the combustion chamber through 72 pairs of impinging injectors angled at 30° to the main axis of the RDRE. An H_2/O_2 pre-detonator was used to ignite the RDRE after fuel and oxidizer were flowing. The detonation was initiated in a 4.60 mm inner diameter stainless steel tube and then tangentially fed into the RDRE combustion chamber 8.90 mm downstream of the fuel injectors. In order to protect the platform and all test apparatus, the tests were limited to 500 ms duration and the RDRE fuel and oxidizer manifolds and combustion chamber were flushed with nitrogen before and after every test. Further detailed information on this test platform can be found in [24].

4.2 Optical Setup

In order to facilitate the addition of several sensors near the exhaust plane of the RDRE, an extension ring was added (See Figure 4.1) to the outer body of the RDRE. The extension ring was fastened to the RDRE by the eight threaded rods that already held the RDRE assembly together. Because of this, any sensor ports had to fit into the limited space between each of those rods. Gland grooves were placed on the axial surfaces of the extension ring to seal the extension ring to the RDRE outer body and so that the same leak check hardware could be used with the extension ring in place. The inner radius of the extension ring was matched to that of the RDRE combustion chamber and the length added to the RDRE by the ring was 0.875 in. This was chosen to be as small as possible in order to minimize

the change to the RDRE geometry and aero-acoustical dynamics. Since a similar extension could not be made for the inner body, a completely new longer inner body was made. Small flat sections were machined into the outer surface of the inner body to line up with the sensor ports to solve the issue of beam spreading from reflection off of a curved surface. Four sensor ports were spaced at 90° around the extension ring. Each port was fitted with a plug that was either blank or held a window (See Figure 4.2). The blank plugs' inner surface exactly matches the inner curve of the extension ring. The window plugs each had a central bore 0.39 in in diameter through the middle and could hold a 0.5 in optical window at the inner tip. The window was glued into the window plug using a high temperature epoxy. The windows used were wedged to reduce etalon effects and were made from either sapphire (un-coated or AR coated for 2-5 μm) or UV fused silica depending on the sensor used in that port. Only un-coated sapphire and fused silica worked well as the window coatings burned off quickly during the RDRE tests. The window plugs also had four #4-40 threaded holes in the outer surface, spaced to interface with Thorlabs 16 mm optical cage hardware. The plugs were attached to the extension ring via two #8-32 bolts for easier removal and swapping of sensors and plugs. Figure 4.6 shows the engine with the extension ring in place and all four sensors installed.

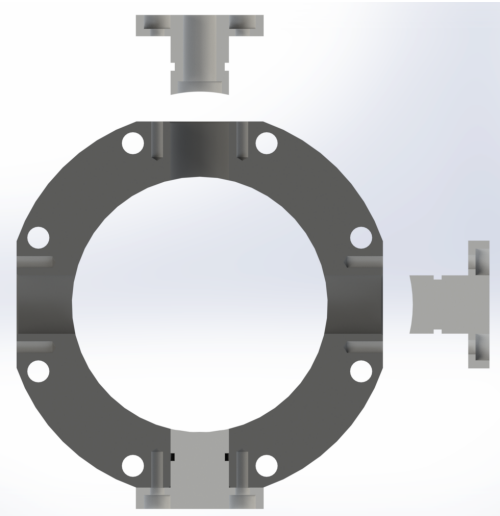

Figure 4.1. RDRE Extension Ring cross section with window and blank plugs

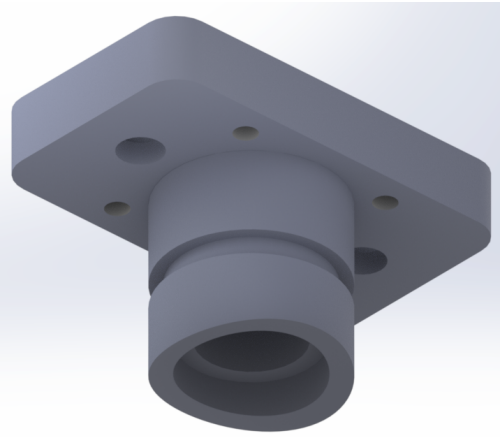

Figure 4.2. RDRE Window Holder

The general shape and structure of the sensor's optical hardware is based on previous designs for TDLAS sensors deployed in RDEs such as in [5]. The RDRE in this study is roughly half the size of the one used by Peng et al. [5], so some design changes were needed. One of the more major differences is this sensor's use of a fiber collimation package for beam re-collimation out of the fiber versus Peng et al.'s use of an off-axis parabolic mirror setup. Furthermore, this sensor used both Thorlabs's 16 mm and 30 mm optical cage hardware systems to reduce the footprint of the sensor on the RDRE and thereby minimize the length needed for the extension ring. Figure 4.5 details the optical hardware setup and shows the beam path for the sensor. The laser beam is supplied to the sensor via a fiber optic cable and then re-collimated using a fiber collimation package. The beam is directed off of a 3 mm right angle prism mirror and down through the center hole in the mirror plug. The beam passes through the window, crosses the annular gap and is reflected off of the RDRE inner body. The beam then passes back through the window, travels past the mirror, through an iris, and then through a lens which focuses it onto the detector. An exploded view of the optical hardware assembly is show in Figure 4.3. The assembled hardware is also shown in Figure 4.4.

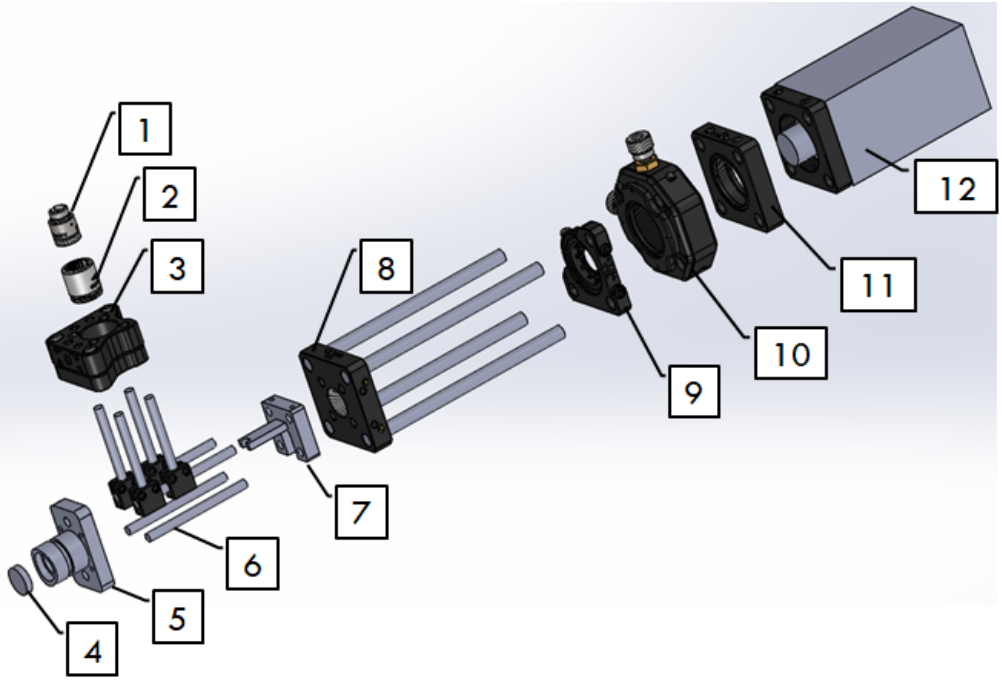

Figure 4.3. Exploded view of optical hardware for single-ended LAS sensor.

1	Fiber collimator	7	Mirror Holder
2	Mount adaptor	8	ThorLabs 30 mm cage system
3	Angle kinematic mount	9	Iris
4	1/2 in. window	10	XY kinematic mount for Lens
5	Window plug	11	Band pass filter
6	ThorLabs 16 mm cage system	12	Detector

4.2.1 Design of Optical Cage System

While the adjustable nature of many of the optical cage hardware components allow for some flexibility in design, there were many limitations and restrictions that needed to be accounted for. For example, the angle adjustment on fiber collimator mount is limited to $\pm 4°$ and the X-Y mount holding the lens is limited to ± 1 mm of travel. While these and various other dimensions of the cage hardware setup could be reconfigured on the fly, the dimensions of the right angle mirror holder could not and the position of the mirror relative to the other elements needed to be designed from the start. Additionally, while it would have been more optimal to have the focusing lens as close to the top of the window holder as possible, there needed to be space beneath it for the entire 16 mm cage system setup, particularly for the

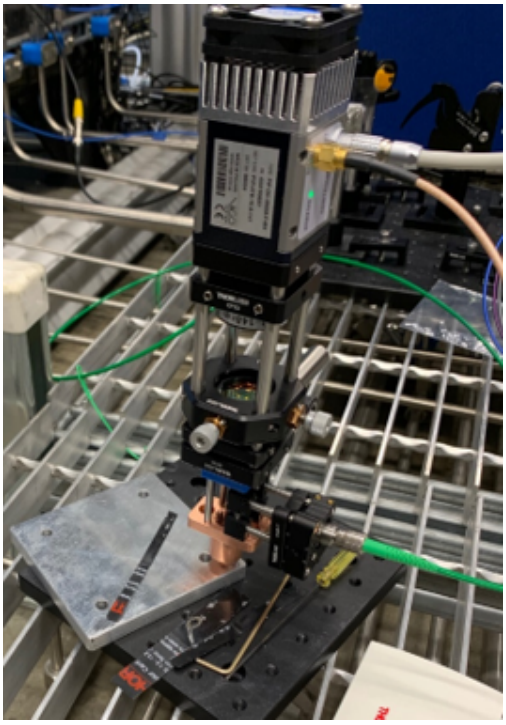

Figure 4.4. Optical hardware stack with window plug for single-ended LAS sensor.

16 mm cage right angle adapters to hold the beam collimation section. A particularly tricky design constraint was to maximize the amount of the return beam that got focused onto the detector while minimizing the amount of spurious reflections also landing on the detector.

4.2.2 Fiber Coupling QCL

In order to distance the QCL from the RDRE, the QCL was placed on a small breadboard and the laser was directed off of two adjustment mirrors and coupled into a 2 meter long 9 μm single-mode InF_3 fiber (Thorlabs P3-32F-FC-2) via a FiberPort (Thorlabs PAF2-4E). The laser was re-collimated out of the fiber via a collimation package (Thorlabs F028APC-4950) attached to the sensor's cage system. Sufficient space was left on the breadboard between the mirrors and the FiberPort to place either additional optical filters used for adjusting overall beam power or a Germanium etalon used to characterize the wavelength tuning of the sensor. The fiber coupling setup is shown below in Figure 4.7, and the specific laser and controllers used are shown below in Table 4.1.

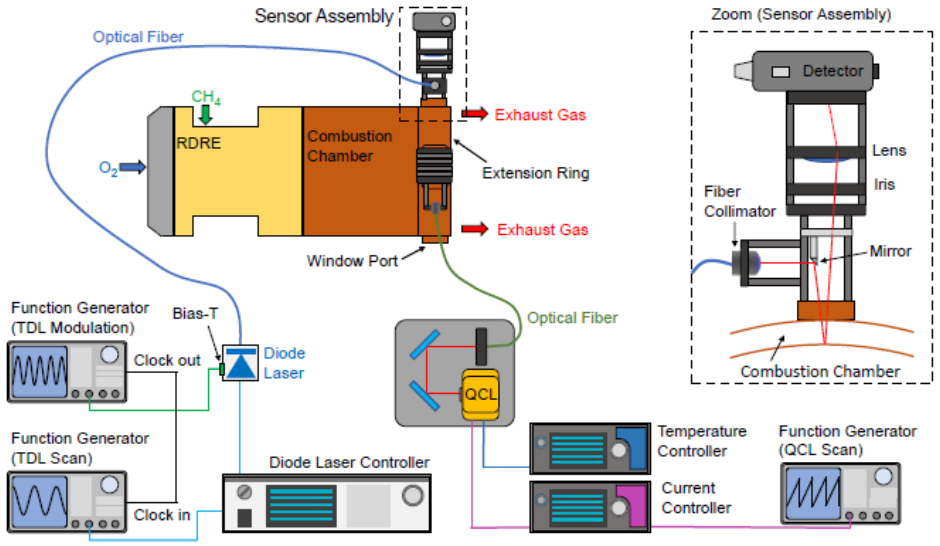

Figure 4.5. Optical setup for single-ended LAS sensors deployed in RDRE. Figure taken from Mathews et al. [1]

Table 4.1. Laser Equipment

	Manufacturer	Product Name
QCL1	Alpes Lasers	HHL-421
QCL2[1]	Alpes Lasers	HHL-726
QCL controller	Wavelength Electronics	QCL500
TEC controller	Wavelength Electronics	TC5

[1]Used in RDRE diagnostic

4.2.3 Ray Tracing

To aid with the designing of the optical hardware setup, a simple ray tracing tool was made in MatLab. For a given setup geometry, the tool iterated through the fine adjustments allowed by the hardware and solved for the beam path. Results from multiple runs were then compared to find the setup with the most margin and largest adjustment window. Additionally, the initial results of the ray tracing tool showed that due to the small diameter of the inner body, the reflected beam would spread too much and it was necessary to have a small flat surface on the inner body.

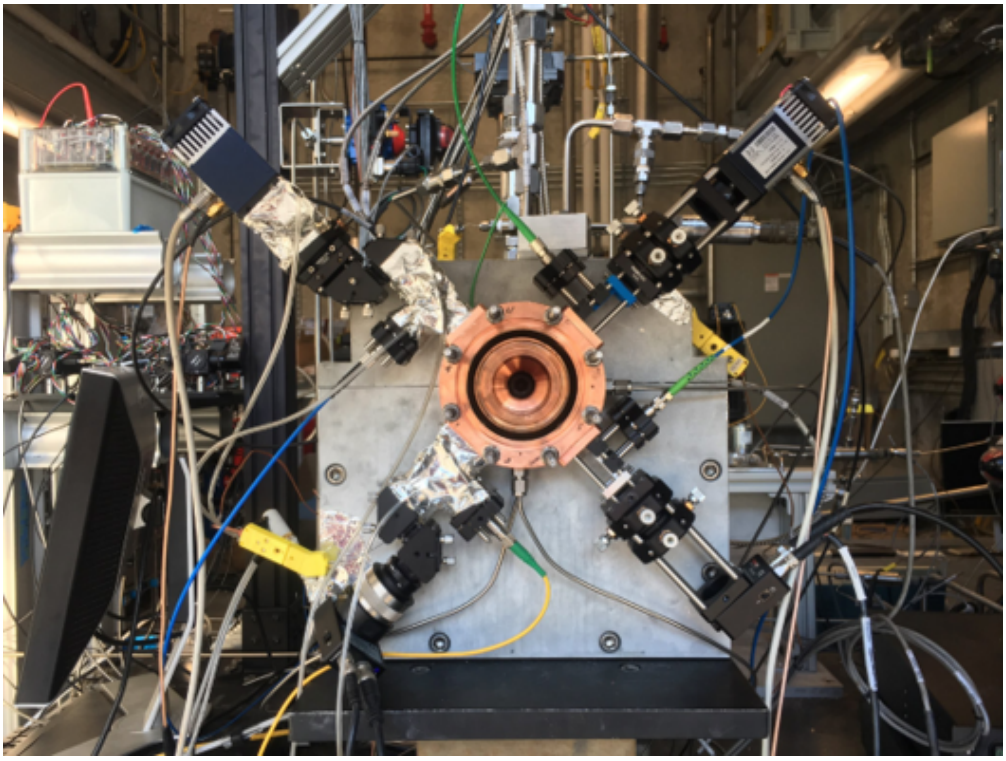

Figure 4.6. Rotating detonation rocket engine with extension ring and four single-ended LAS sensors installed. Mid-IR CO sensor located in top right position.

4.3 Processing Considerations

Additional sources of error and noise present in the *in situ* setup relative to the development tests done in a lab environment reduced the measurement quality enough to necessitate dropping the measurement rate from 1 MHz to 0.75 MHz. A major factor in this was the degradation of the absorption signal due to significant and unpredictable beam steering during the test.

4.3.1 Adding X_{H_2O} to Model for Collisional Width

Calculating the collisional widths for a spectral model can be challenging. It depends on the both the total pressure and the make-up of the bath gas, neither of which is known in this scenario. Often the make-up of the bath gas exactly does not matter as the collisional coefficients for CO-CO_2, CO-N_2, and CO-Air are very similar and so changing mole fractions

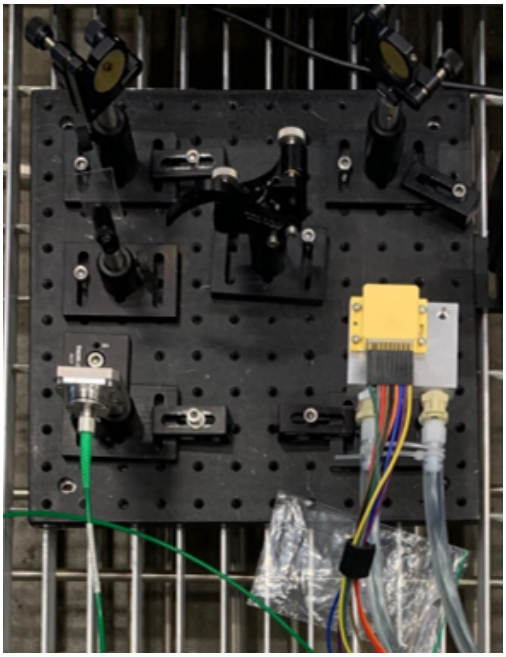

Figure 4.7. QCL and fiber coupling setup on breadboard

of these species does little to affect the total collisional width. However, the presence of water can have a significant effect as the CO-H_2O collisional-broadening coefficient for these lines is much different and scales differently with temperature. The trouble comes with how to control for this. Often the collisional width itself can be changed to a floated parameter in the model or in a model with many lines a $\nu_{\text{c,scaling}}$ parameter can be added to scale all collisional widths together, but in situations like this with highly variable pressure, if pressure is also floated in the model, the two parameters are not able to be differentiated. Instead an assumed static value for X_{H_2O} was used based on measurements taken from an H_2O diagnostic during the same test and on a STANJAN equilibrium calculation at the test conditions.

5. EXPERIMENTAL RESULTS

5.1 Results

A selection of the results is presented below for the case of an equivalence ratio of ϕ=1.77 and total propellant mass flow rate of $\dot{m}$ = 0.6 lb/s. These measurements occurred 310 ms into the test when the RDRE was running at its most stable, with a wave frequency of approximately 11.6 kHz.

Two sample scans are shown below in Figures 5.1 and 5.2. These demonstrate scans at relatively low and high temperatures and pressures, respectively. Note the increase in line width due to increased collisional broadening in the higher pressure spectrum. Even with a broader fundamental band line, the hot band line can still be detected in the model yielding a good fit and accurate prediction of gas conditions.

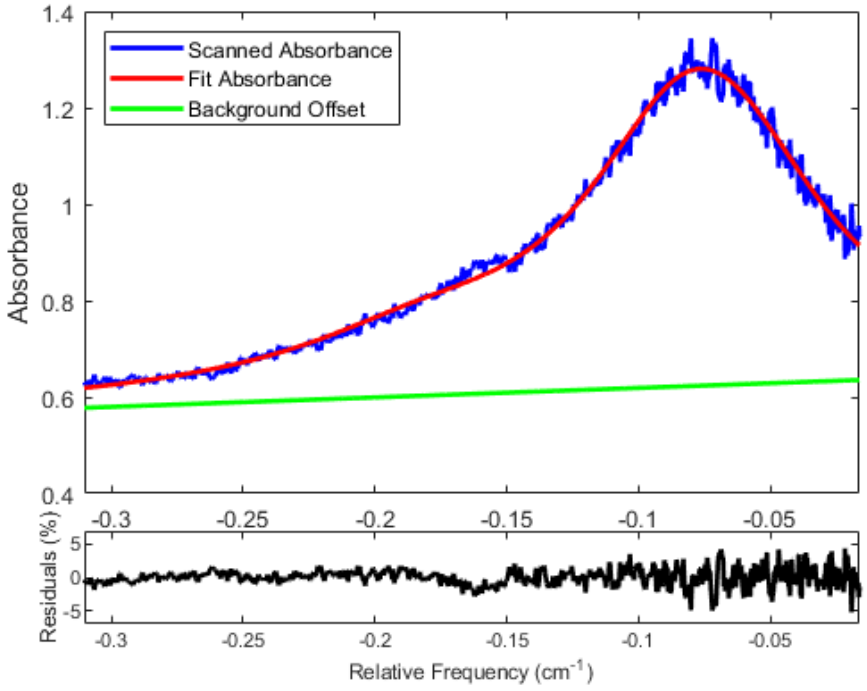

Figure 5.1. Scanned and fit absorbance just before trail of detonation wave passes (t=0.310350s) with peak normalized residuals $\leq$ 5%. Best fit gas conditions are T=1776 $\pm$ 46 K and P=2.703 $\pm$ 0.082 atm (95% CI)

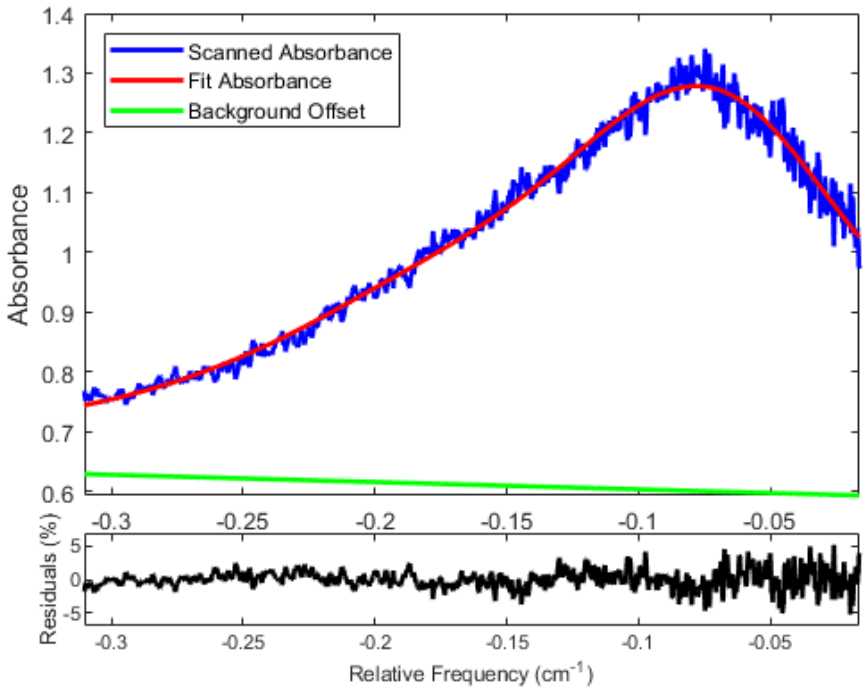

Figure 5.2. Scanned and fit absorbance just after trail of detonation wave passes (t=0.310355s) with peak normalized residuals $\leq 5\%$. Best fit gas conditions are T=2365 $\pm$ 89 K and P=5.391 $\pm$ 0.265 atm (95% CI)

5.1.1 Time History

A time history of measured temperatures and pressures is presented in Figure 5.3. The cyclical behavior of the RDRE is readily apparent. Gas conditions oscillate between 1800-2400 K and 2.5-5.5 atm. A zoomed in one-cycle view of temperature, total pressure, and partial pressure for CO are shown in Figures 5.4, 5.5, and 5.6, respectively, with 95% confidence intervals shown in black. The confidence interval size is correlated with total pressure, but very clear structure and dynamics can be seen with good resolution and precision through out the cycle. The sharp pressure spike as the trail of the detonation wave passes by can clearly be seen and with a measurement rate of 0.75 MHz, the time resolution is sufficient to capture multiple samples during the pressure rise from the wave's passing. The ability to capture this level of detail will be invaluable for studying RDREs and μs-scale combustion dynamics in other environments.

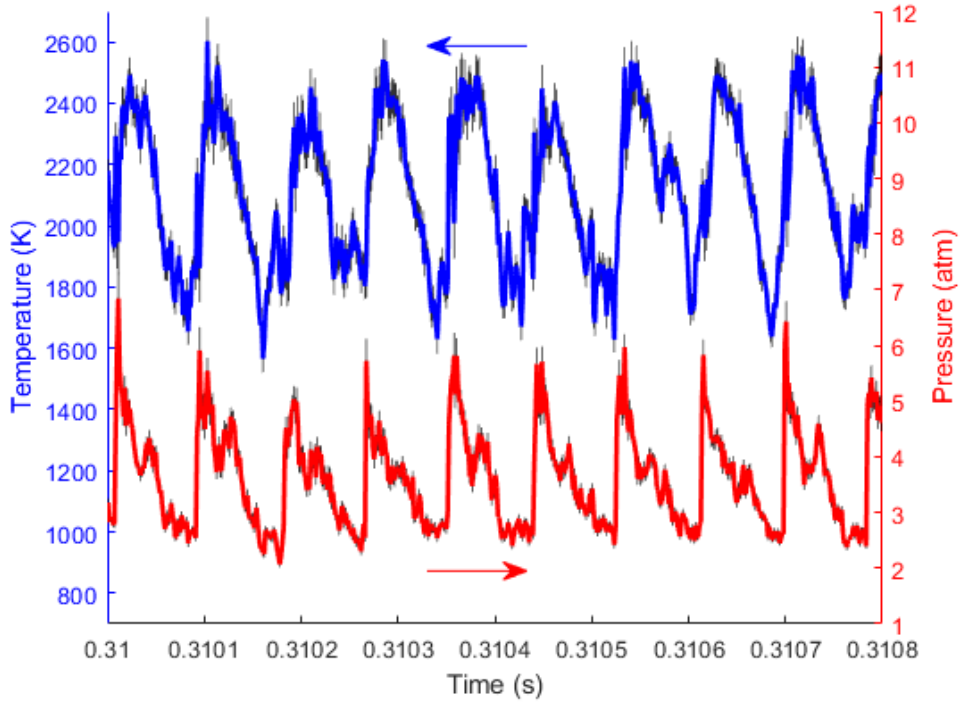

Figure 5.3. Time history of temperature and pressure 310 ms after test start showing RDRE cyclic operation at approximately 11.6kHz. 95% confidence intervals are shown in black.

5.1.2 Cycle Averages

Each cycle of the RDRE is marked by a sharp rise in pressure from the trail of the detonation wave passing by the sensor. This provided a convenient reference point for syncing up all the cycles so that cycle statistics could be gathered. Below in Figures 5.7 and 5.8 are the profiles for the average temperature and pressure cycles with standard deviation measured at the exhaust over a period of 10 ms. These represent the kind of useful statistics that this diagnostic is capable of producing. Note that the standard deviation for the cycles is a combination of measurement error and actual cycle-to-cycle variation. Also of note is the second pressure rise approximately 35 μs into the cycle. Further analysis of these kinds of features may yield insight into the structure of the detonation wave and how it varies in time.

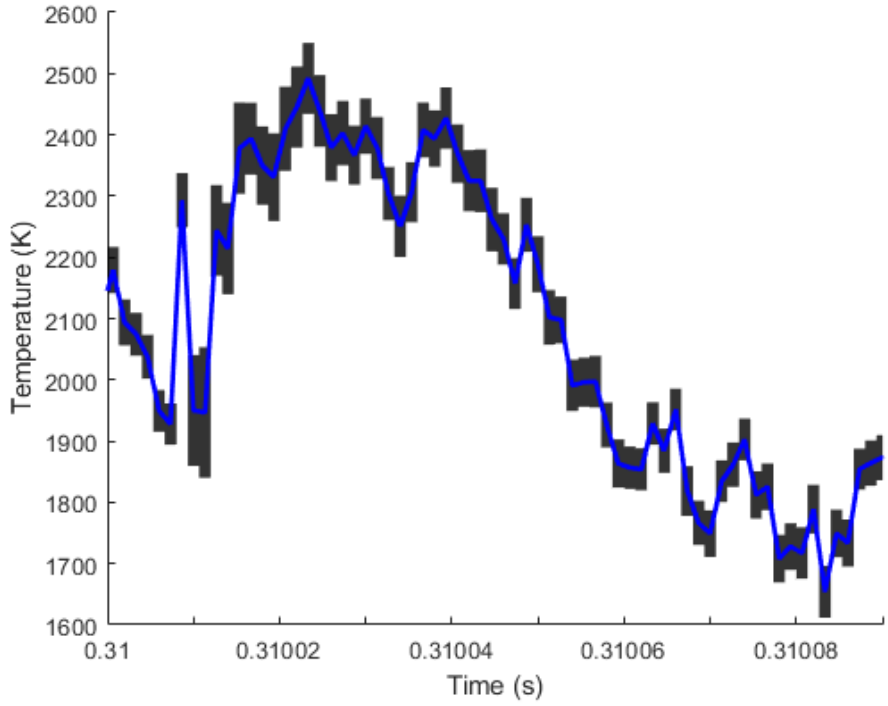

Figure 5.4. Temperature (with 95% CI) during single cycle of RDRE. RMS 95% CI is 97 K.

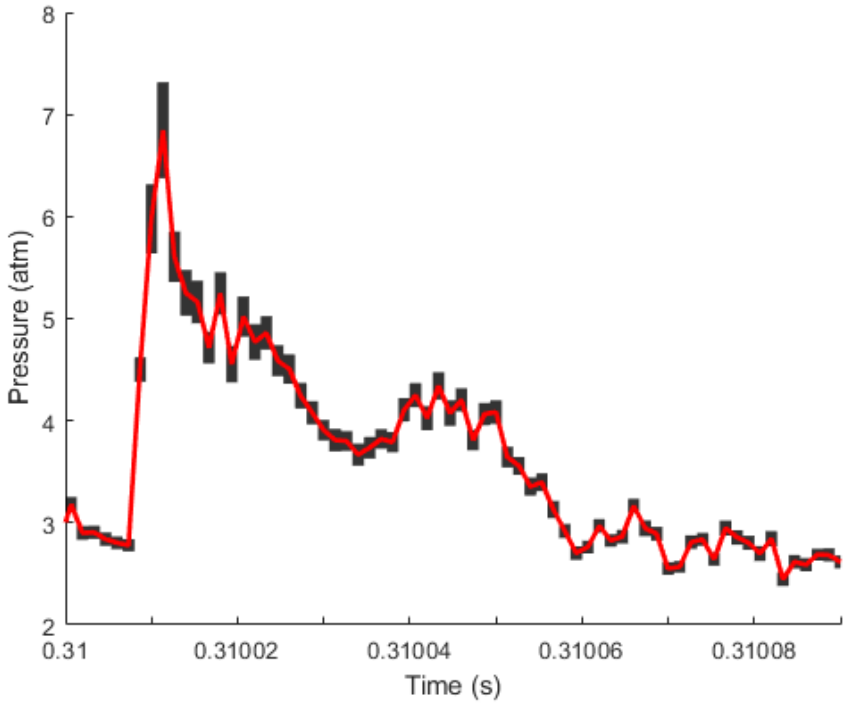

Figure 5.5. Pressure (with 95% CI) during single cycle of RDRE. RMS 95% CI is 0.257 atm.

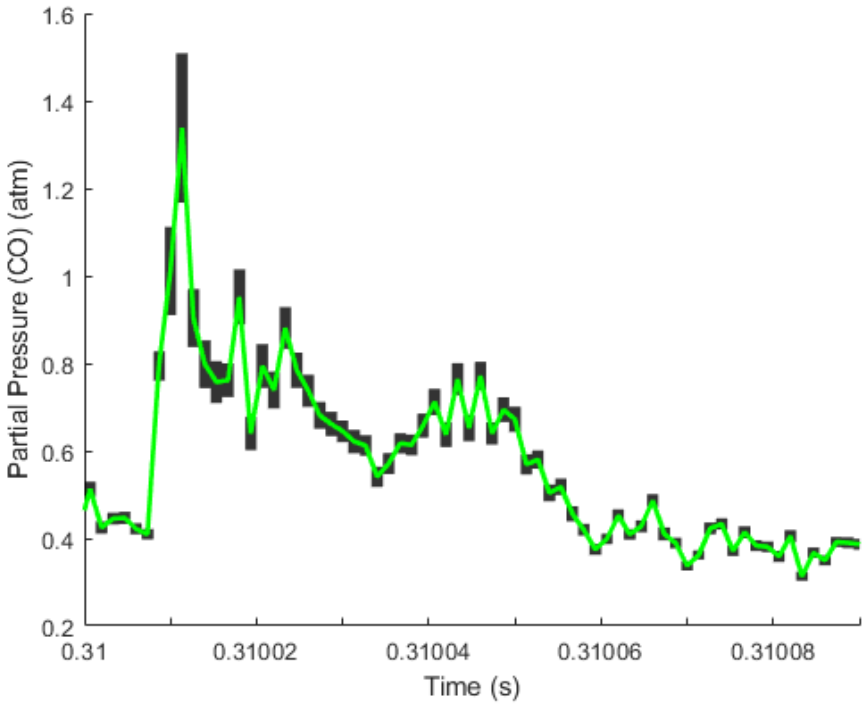

Figure 5.6. Partial pressure of CO (with 95% CI) during single cycle of RDRE. RMS 95% CI is 0.071

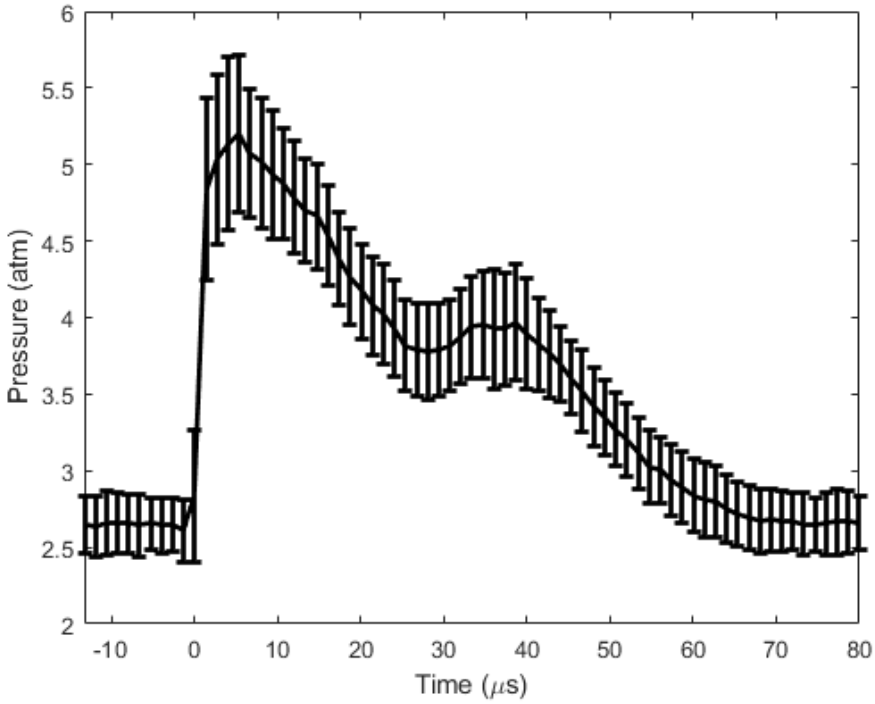

Figure 5.7. Average pressure cycle over first 10 ms.

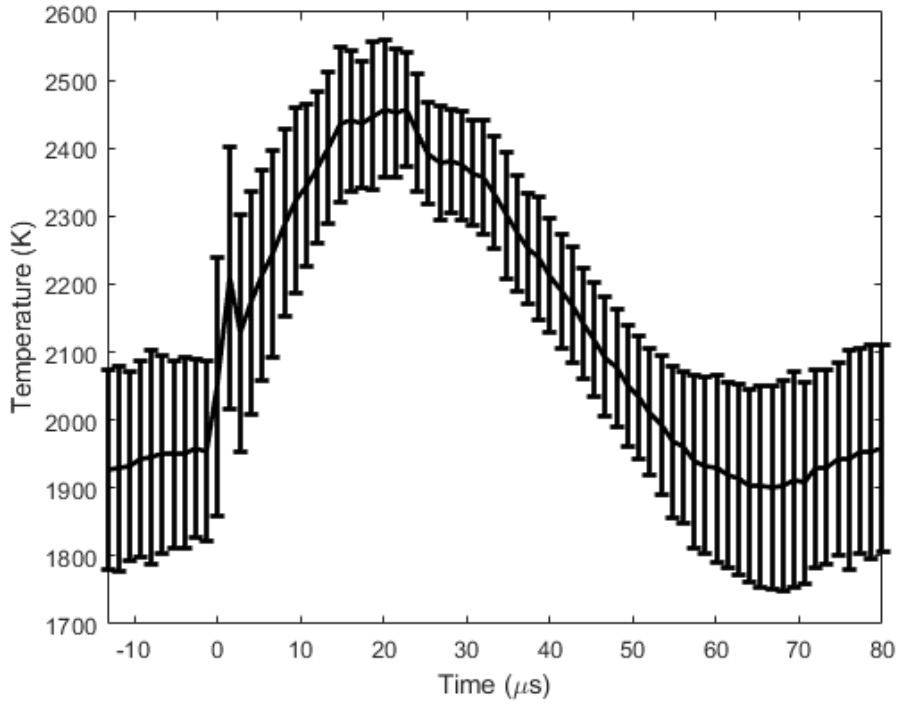

Figure 5.8. Average temperature cycle over first 10 ms.

6. SUMMARY

This thesis presented a laser absorption spectroscopy diagnostic capable of measuring temperature, pressure, and CO in harsh combustion environments such as in the annulus of a rotating detonation rocket engine. This diagnostic utilizes a quantum cascade laser (QCL) at 4.98 μm to scan across a group of CO absorption lines near 2008.5 cm^{-1} at 750 kHz. This diagnostic was used in a series of tests to characterize a methane-oxygen fueled RDRE. An extension ring with multiple sensor ports was designed and attached to the RDRE to allow optical access to the annulus. Additional optical hardware was connected to the extension ring to deliver the fiber-coupled QCL beam to the annulus and to collect and detect the laser light reflected off of the RDRE inner body. Results from the test case where $\phi = 1.77$ and $\dot{m} = 0.6$ lb/s were shown. This diagnostic demonstrated precise measurements with 95% confidence intervals for both temperature and pressure of $< 10\%$, even at elevated temperatures (2500 K) and pressures (6 atm). The presented diagnostic is the first of its kind to permit mid-infrared measurement of CO inside an RDRE annulus at repetition rates > 100 kHz. It has been demonstrated that this diagnostic is capable of capturing the dynamic gas conditions inside the annulus of an RDRE which will enable further detailed study of RDRE operation and the combustion physics governing these devices.

REFERENCES

[1] Garrett C. Mathews, Matthew Blaisdell, Aaron I. Lemcherfi, Carson D. Slabaugh, and Christopher S. Goldenstein. "High-Bandwidth Laser-Absorption Measurements of Temperature, Pressure, CO, and H_2O in the Annulus of a Rotating Detonation Rocket Engine". In: *AIAA Scitech 2021 Forum* (2021). DOI: 10.2514/6.2021-0418.

[2] Christopher S Goldenstein, Christopher A Almodóvar, Jay B Jeffries, Ronald K Hanson, and Christopher M Brophy. "High-bandwidth scanned-wavelength-modulation spectroscopy sensors for temperature and H_2O in a rotating detonation engine". In: *Measurement Science and Technology* 25.10 (), p. 105104. DOI: 10.1088/0957-0233/25/10/105104.

[3] Keith D. Rein, Sukesh T. Roy, Scott W. Sanders, Andrew R. Caswell, Frederick R. Schauer, and James Gord. "Measurements of gas temperatures at 100 kHz within the annulus of a rotating detonation engine". In: *Applied Physics B* 123.88 (2017), pp. 1–9. DOI: 10.1007/s00340-017-6647-5.

[4] Andrew W. Caswell, Sukesh Roy, Xinliang An, Scott T. Sanders, Frederick R. Schauer, and James R. Gord. "Measurements of multiple gas parameters in a pulsed-detonation combustor using time-division-multiplexed Fourier-domain mode-locked lasers". In: *Applied Optics* 52.12 (2013), pp. 2893–2904. DOI: 10.1364/AO.52.002893.

[5] Wen Yu Peng, Séan J. Cassady, Christopher L. Strand, Christopher S. Goldenstein, R. Mitchell Spearrin, Christopher M. Brophy, Jay B. Jeffries, and Ronald K. Hanson. "Single-ended mid-infrared laser-absorption sensor for time-resolved measurements of water concentration and temperature within the annulus of a rotating detonation engine". In: *Proceedings of the Combustion Institute* 37.2 (2019), pp. 1435 –1443. DOI: https://doi.org/10.1016/j.proci.2018.05.021.

[6] Sean J. Cassady, Wen Yu Peng, Christopher L. Strand, Jay B. Jeffries, Ronald K. Hanson, David F. Dausen, and Christopher M. Brophy. "A single-ended, mid-IR sensor for time-resolved temperature and species measurements in a hydrogen/ethylene-fueled rotating detonation engine". In: *AIAA Scitech 2019 Forum* (2019). DOI: 10.2514/6.2019-0027.

[7] Garrett C. Mathews and Christopher S. Goldenstein. "Wavelength-Modulation Spectroscopy for MHz Thermometry and H_2O Sensing in Combustion Gases of Energetic Materials". In: *AIAA Scitech 2019 Forum* (2019). DOI: 10.2514/6.2019-1609.

[8] Garrett C. Mathews and Christopher S. Goldenstein. "Wavelength-Modulation-Spectroscopy Diagnostics for Characterizing Metallized and Halogenated Fireballs of Energetic Materials". In: *AIAA Scitech 2020 Forum* (2020). DOI: 10.2514/6.2020-0301.

[9] Garrett Mathews and Christopher Goldenstein. "Near-GHz scanned-wavelength-modulation spectroscopy for MHz thermometry and H_2O measurements in aluminized fireballs of energetic materials". In: *Applied Physics B* 126.11 (2020), pp. 1–17. DOI: 10.1007/s00340-020-07527-z.

[10] Anil P. Nair, Daniel D. Lee, Daniel I. Pineda, Jason Kriesel, William A. Hargus, John W. Bennewitz, Stephen A. Danczyk, and R. Mitchell Spearrin. "MHz laser absorption spectroscopy via diplexed RF modulation for pressure, temperature, and species in rotating detonation rocket flows". In: *Applied Physics B* 126.8 (2020), pp. 1–20. DOI: 10.1007/s00340-020-07483-8.

[11] Anil P. Nair, Christopher Jelloian, David S. Morrow, Fabio A. Bendana, Daniel I. Pineda, and Raymond M. Spearrin. "MHz mid-infrared laser absorption sensor for carbon monoxide and temperature behind detonation waves". In: *AIAA Scitech 2020 Forum* (2020). DOI: 10.2514/6.2020-0733.

[12] Anil P. Nair, Daniel Lee, Daniel Pineda, Raymond M. Spearrin, Jason Krisel, William A. Hargus, John W. Bennewitz, and Stephen Danczyk. "MHz Mid-infrared Laser Absorption of CO and CO_2 for Pressure, Temperature, and Species in Rotating Detonation Rocket Flows". In: *AIAA Propulsion and Energy 2020 Forum* (2020). DOI: 10.2514/6.2020-3867.

[13] Christopher S. Goldenstein, Ian A. Schultz, Jay B. Jeffries, and Ronald K. Hanson. "Two-color absorption spectroscopy strategy for measuring the column density and path average temperature of the absorbing species in nonuniform gases". In: *Applied Optics* 52.33 (2013), pp. 7950–7962. DOI: 10.1364/AO.52.007950.

[14] I.E. Gordon, L.S. Rothman, C. Hill, R.V. Kochanov, Y. Tan, P.F. Bernath, M. Birk, V. Boudon, A. Campargue, K.V. Chance, B.J. Drouin, J.-M. Flaud, R.R. Gamache, J.T. Hodges, D. Jacquemart, V.I. Perevalov, A. Perrin, K.P. Shine, M.-A.H. Smith, J. Tennyson, G.C. Toon, H. Tran, V.G. Tyuterev, A. Barbe, A.G. Császár, V.M. Devi, T. Furtenbacher, J.J. Harrison, J.-M. Hartmann, A. Jolly, T.J. Johnson, T. Karman, I. Kleiner, A.A. Kyuberis, J. Loos, O.M. Lyulin, S.T. Massie, S.N. Mikhailenko, N. Moazzen-Ahmadi, H.S.P. Müller, O.V. Naumenko, A.V. Nikitin, O.L. Polyansky, M. Rey, M. Rotger, S.W. Sharpe, K. Sung, E. Starikova, S.A. Tashkun, J. Vander Auwera, G. Wagner, J. Wilzewski, P. Wcisło, S. Yu, and E.J. Zak. "The HITRAN2016 molecular spectroscopic database". In: *Journal of Quantitative Spectroscopy and Radiative Transfer* 203 (2017). HITRAN2016 Special Issue, pp. 3–69. DOI: https://doi.org/10.1016/j.jqsrt.2017.06.038.

[15] Ronald K. Hanson, R. Mitchell Spearrin, and Christopher S. Goldenstein. *Spectroscopy and Optical Diagnostics for Gases*. Springer International Publishing, 2016.

[16] Christopher S. Goldenstein, Victor A. Miller, R. Mitchell Spearrin, and Christopher L. Strand. "SpectraPlot.com: Integrated spectroscopic modeling of atomic and molecular gases". In: *Journal of Quantitative Spectroscopy and Radiative Transfer* 200 (2017), pp. 249–257. DOI: https://doi.org/10.1016/j.jqsrt.2017.06.007.

[17] L.S. Rothman, I.E. Gordon, R.J. Barber, H. Dothe, R.R. Gamache, A. Goldman, V.I. Perevalov, S.A. Tashkun, and J. Tennyson. "HITEMP, the high-temperature molecular spectroscopic database". In: *Journal of Quantitative Spectroscopy and Radiative Transfer* 111.15 (2010). XVIth Symposium on High Resolution Molecular Spectroscopy (HighRus-2009), pp. 2139–2150. DOI: https://doi.org/10.1016/j.jqsrt.2010.05.001.

[18] Kevin K. Schwarm, Huy Q. Dinh, Christopher S. Goldenstein, Daniel I. Pineda, and R. Mitchell Spearrin. "High-pressure and high-temperature gas cell for absorption spectroscopy studies at wavelengths up to 8 μm". In: *Journal of Quantitative Spectroscopy and Radiative Transfer* 227 (2019), pp. 145–151. DOI: https://doi.org/10.1016/j.jqsrt.2019.01.029.

[19] John W. Bennewitz, Blaine R. Bigler, William A. Hargus, Stephen A. Danczyk, and Richard D. Smith. "Characterization of Detonation Wave Propagation in a Rotating Detonation Rocket Engine using Direct High-Speed Imaging". In: *2018 Joint Propulsion Conference*. DOI: 10.2514/6.2018-4688.

[20] John W. Bennewitz, Blaine R. Bigler, Jessica J. Pilgram, and Jr. William A. Hargus. "Modal Transitions in Rotating Detonation Rocket Engines". In: *International Journal of Energetic Materials and Chemical Propulsion* 18.2 (2019), pp. 91–109.

[21] Blaine R. Bigler, John W. Bennewitz, Stephen A. Schumaker, Stephen A. Danczyk, and William A. Hargus. "Injector Alignment Study for Variable Mixing in Rotating Detonation Rocket Engines". In: *AIAA Scitech 2019 Forum*. DOI: 10.2514/6.2019-2019.

[22] William A. Hargus, Stephen A. Schumaker, and Eric J. Paulson. "Air Force Research Laboratory Rotating Detonation Rocket Engine Development". In: *2018 Joint Propulsion Conference*. DOI: 10.2514/6.2018-4876.

[23] Richard D. Smith and Steven Stanley. "Experimental Investigation of Continuous Detonation Rocket Engines for In-Space Propulsion". In: *52nd AIAA/SAE/ASEE Joint Propulsion Conference*. DOI: 10.2514/6.2016-4582.

[24] Kyle Schwinn, Rohan Gejji, Brandon Kan, Swanand Sardeshmukh, Stephen Heister, and Carson D. Slabaugh. "Self-sustained, high-frequency detonation wave generation in a semi-bounded channel". In: *Combustion and Flame* 193 (2018), pp. 384 –396. DOI: https://doi.org/10.1016/j.combustflame.2018.03.022.